The Astrophysical Journal, 874:57 (13pp), 2019 March 20 https://doi.org/10.3847/1538-4357/ab06f2

The Evolution of Magnetic Rayleigh–Taylor Unstable Plumes and Hybrid KH-RT Instability into a Loop-like Eruptive Prominence

Sudheer K. Mishra and A. K. Srivastava
Department of Physics, Indian Institute of Technology (BHU), Varanasi-221005, India; sudheerkm.rs.phy16@itbhu.ac.in
Received 2018 December 20; revised 2019 February 12; accepted 2019 February 12; published 2019 March 21

Abstract

MRT-unstable plumes are observed in a loop-like eruptive prominence using *Solar Dynamic Observatory*/Atmospheric Imaging Assembly observations. The small-scale cavities are developed within the prominence, where perturbations trigger dark plumes (P1 and P2) propagating with speeds of 35–46 km s^{-1}. The self-similar plume formation initially shows the growth of a linear MRT-unstable plume (P1), and thereafter the evolution of a nonlinear single-mode MRT-unstable second plume (P2). A differential emission measure analysis shows that plumes are less dense and hotter than the prominence. We have estimated the observational growth rate for both plumes as $1.32 \pm 0.29 \times 10^{-3}\,s^{-1}$ and $1.48 \pm 0.29 \times 10^{-3}\,s^{-1}$, respectively, which are comparable to the estimated theoretical growth rate ($1.95 \times 10^{-3}\,s^{-1}$). The nonlinear phase of an MRT-unstable plume (P2) may collapse via a Kelvin–Helmholtz vortex formation in the downfalling plasma. Later, a plasma thread is evident in the rising segment of this prominence. It may be associated with the tangled field and Rayleigh–Taylor instability. The tangled field initiates shearing at the prominence–cavity boundary. Due to this shear motion, the plasma downfall occurred at the right part of the prominence–cavity boundary. It triggers the characteristic KH unstable vortices and MRT-unstable plasma bubbles propagating at different speeds and merging with each other. The shear motion and lateral plasma downfall may initiate hybrid KH-RT instability there.

Key words: instabilities – Sun: corona

Supporting material: animations

1. Introduction

Solar prominences are the clouds of cool and dense plasma materials that are suspended over the less dense and hot coronal plasma with the support of the magnetic field. The various classifications that describe the formation of prominences depend on the morphology, location, activity, and behavior of the photospheric magnetic field (e.g., Tandberg-Hanssen 1998; Parenti 2014). The formation of prominences can be classified according to location. For example, consider active regions, annd intermediate and quiescent prominences. All three are associated with the photospheric magnetic field of the Sun. The active region prominences are associated with the strong magnetic field and their polarity inversion lines develop around the sunspots. Of the three, active region prominences have the largest magnetic energy, therefore they are more unstable. The quiescent prominences are the most stable. They form in the higher latitude regions and are associated with weaker photospheric magnetic fields (Priest 1989). The quiescent prominences have a lifetime of a few hours to more than a week because of their larger spatial scale. Due to the highly dynamic behavior of the quiescent prominences, they demonstrate different irregular motions, structuring, and morphological evolution of the plasma structures, and large-scale and small-scale flows during their lifetimes. The quiescent prominences consist of plasma bubbles, which were first observed by Stellmacher & Wiehr (1973), and later they were found to be Rayleigh–Taylor unstable (e.g., Berger et al. 2010; Ryutova et al. 2010). The quiescent prominences possess some interesting properties like internal plasma downfall, plumes, plasma bubbles, plasma blobs, finger structures, and mushroom-like structures (e.g., Berger et al. 2008, 2010; Ryutova et al. 2010; Schmieder et al. 2010). Plumes, plasma bubbles, plasma blobs, and other small-scale features have never been observed in the active region and intermediate prominences. These morphological structures have been used to understand the internal dynamics and magnetic configuration of various prominences, and they may be linked to the different types of instabilities.

The Rayleigh–Taylor instability was initially suggested by Rayleigh (1899) and Taylor (1950) to discuss the behavior of two fluids when a small perturbation acts on the interface of the fluid. Rayleigh–Taylor instability occurrs when a denser fluid is supported above a low denser fluid and they are accelerated against gravity. The horizontal component of the magnetic field acting on the interface gives the directionality of the magnetic Rayleigh–Taylor instability. *HINODE*/SOT data have been used to understand the thermal and magnetic causes of the formation of the plume within a hedgerow quiescent prominence (Berger et al. 2008). Later they observed that these plumes formed due to the magnetic Rayleigh–Taylor instability (Berger et al. 2010). A three-dimensional numerical simulation has been performed to observe the magnetic Rayleigh–Taylor instability in the filamentary structures (e.g., Jun et al. 1995; Isobe et al. 2005). Various magnetic field configurations have been used to study the growth rate of MRT-unstable fingers and plasma bubbles (Stone & Gardiner 2007). The turbulent dark upflow originates from the base of the quiescent prominences, and ejection of the plasma blobs associated with the prominence threads has been observed using SOT data (Hillier et al. 2011a, 2011b). Similar turbulent dark upflows have been observed into the hedgerow quiescent prominence using SOT data, which were found to be the magnetic Rayleigh–Taylor unstable plumes (e.g., Berger et al. 2008, 2010; de Toma et al. 2008; Ryutova et al. 2010). Later numerical simulation have also been performed to study the nonlinear stability of the Kippehahn & Schluter model prominence. It was shown that

the turbulent dark upflows and the reconnection-generated downflows also occur into these prominences. Such plasma dynamics is found to be related to the magnetic Rayleigh–Taylor instability (Hillier et al. 2012a, 2012b).

van Ballegooijen & Cranmer (2010) proposed that the hedgreow prominences consist of large numbers of thin vertical threads supported by a tangled magnetic field. These vertical threads possibly formed due to Rayleigh–Taylor instability associated with the tangled field. They consist of a collection of fine thin structures with widths of a few hundred kilometers to a few thousand kilometers (e.g., Lin et al. 2005; Okamoto et al. 2007.; Chae et al. 2008; Chae 2010). Magnetic field shear affects the growth rate of Rayleigh–Taylor instability, but it does not completely suppress the instability (Ruderman et al. 2014; Zhou 2017a, 2017b). Ryutova et al. (2010) hypothesized that all the plumes in a prominence do not form due to the magnetic Rayleigh–Taylor instability. Some plumes may also have formed due to the Kelvin–Helmholtz instability by a strong shear flow at the bubble–prominence interface. Multi-mode plume formation is the cause of magnetic Rayleigh–Taylor instability, while single-mode plume formation is caused by Kelvin–Helmholtz instability. The magnetic Kelvin–Helmholtz unstable vortex-like structures are formed at the surface of fast coronal mass ejection (Foullon et al. 2011, 2013). Ofman & Thompson (2011) observed that the magnetic Kelvin–Helmholtz unstable vortices develop at the boundary of the erupting region and surrounding corona. The characteristics of the prominence–bubble boundary and the effect of the shear flows at the boundary are known (Berger et al. 2017). The strong shear flows along the bubble–prominence interface leads the coupled Kelvin–Helmholtz & Rayleigh–Taylor (KH-RT) instability.

Apart from isolated prominences, the signature of MRT instability has also been observed during their eruptions and even in the outer corona and heliosphere. A massive prominence eruption was observed in the solar atmosphere at 2011 June 7th, and is associated with M2.5 solar flares and erupted out from AR 11226 and AR 11227 (Cheng et al. 2012a, 2012b; Yardley et al. 2016). In this prominence, the plasma downfalls have been observed and these falling plasma blobs consist of magnetic Rayleigh–Taylor unstable arcs, fingers, horns, and spikes as observed in the lower corona (Innes et al. 2012; Carlyle et al. 2014). These MRT-unstable fingers were observed in the intermediate corona in the form of MRT-unstable finger structures and in lower interplanetary space, where they are fragmented into plasma spikes (Mishra et al. 2018a, 2018b). Hillier (2018) reviewed the role of magnetic Rayleigh–Taylor instability in the formation the solar prominences and discussed the linear phase and nonlinear dynamics of MRT instability. Such instability can also be utilized for the magnetic field estimation of these prominences.

To the best of our knowledge, this work is the first effort to understand the dynamics of the magnetic Rayleigh–Taylor unstable plumes and hybrid KH-RT instability, which is associated with the tangled thread in the loop-like eruptive prominence. The details of these MRT-unstable multiple localized small-scale plasma structures (two plumes, one thread, shearing motions, multiple plasma blobs) in the eruptive prominence are described throughout the paper. The observations and data analysis are discussed in Section 2. Section 3 describes the observational results corresponding to the MRT-unstable plumes. The evolution of plasma threads and combined KH-RT instability is discussed in Section 4. In the final section, we provide a discussion and conclusions.

2. Data and Analysis

The *Solar Dynamic Observatory* (*SDO*) consists of three instruments, the Atmospheric Imaging Assembly (AIA), the Heliospheric Magnetic Imager, and the Extreme Ultraviolet Variability Experiment (EVE). We analyze the data from AIA (Lemen et al. 2012). AIA has seven extreme ultraviolet (94, 131, 171, 193, 211, 304, 335 Å), two ultraviolet (1600, 1700 Å), and a visible (4500 Å) full disk imager with a 1.5 arcsec spatial resolution and 12 s temporal resolution. WE downloaded the *SDO*/AIA data from the Joint Science Operation Center (http://jsoc.stanford.edu/) to analyze the prominence eruption. We used the 94 Å, 131 Å, 171 Å, 193 Å, 211 Å, 304 Å, and 335 Å temporal image data of AIA for our analysis. We have selected 3 hr time-sequence data starting from 2014 November 18th. The basic calibration and normalization of the data were performed using the Solarsoft IDL routine "aia_prep.pro."

The AIA images are further processed in order to resolve the finer structures, dynamical features on different spatial scales in the eruptive prominence. Each image is convolved with a Gaussian kernel. The convolved images are subtracted from the normal intensity image to obtain features with better contrast. The same process has been used five times to measure the uncorrelated noise. The uncorrelated noise is subtracted from the original images. The normalized multiscale Gaussian filter is used to enhance the fine structures (e.g., Morgan & Druckmüller 2014; Pant et al. 2015). We select the width of the Gaussian filter as [50, 100, 150, 200, 250] pixels. The filtered images are added to the original data. The MRT-unstable plumes, prominence thread, vortex formation, and shear motion became detectable in the processed images. Therefore, we perform the analysis using the multi-Gaussian filtered images.

The thermal properties of the prominence plasma can be understood by estimating the differential emission measure (DEM). We map the DEM with different temperatures from the six AIA filters, i.e., 94 Å, 131 Å, 171 Å, 193 Å, 211 Å, 304 Å. We adopt the method of Cheung et al. (2015) to measure the emission (EM) from the prominence and surrounding regions. Their method is based on the concept of sparse inversion and uses the "simplex" function to minimize the total emission (EM). The sparse inversion technique gives the positive solutions lying between max(0, I−tol) and (I+tol), where tol is the tolerance in the reconstructed intensities. For the sparse inversion, we divide the range of temperatures between $\log T$ (K) = 4.7–7.2 with 25 temperature bins at $\Delta \log T$(K) = 0.1 intervals. Using the DEM analysis, we identify the cool prominence visible in the temperature range $\log T$ (K) = 4.7–5.0. A major portion of the emission in this temperature range is observed by the *SDO*/AIA 304 Å filter. The dark plumes and cavity regions are clearly observed in the range $\log T$(K) = 5.8–6.1, which corresponds to the AIA 171 Å filter. To estimate the density, we use the estimated total emission coming from different temperature regions:

$$n = \sqrt{\frac{\mathrm{EM}}{l}}, \tag{1}$$

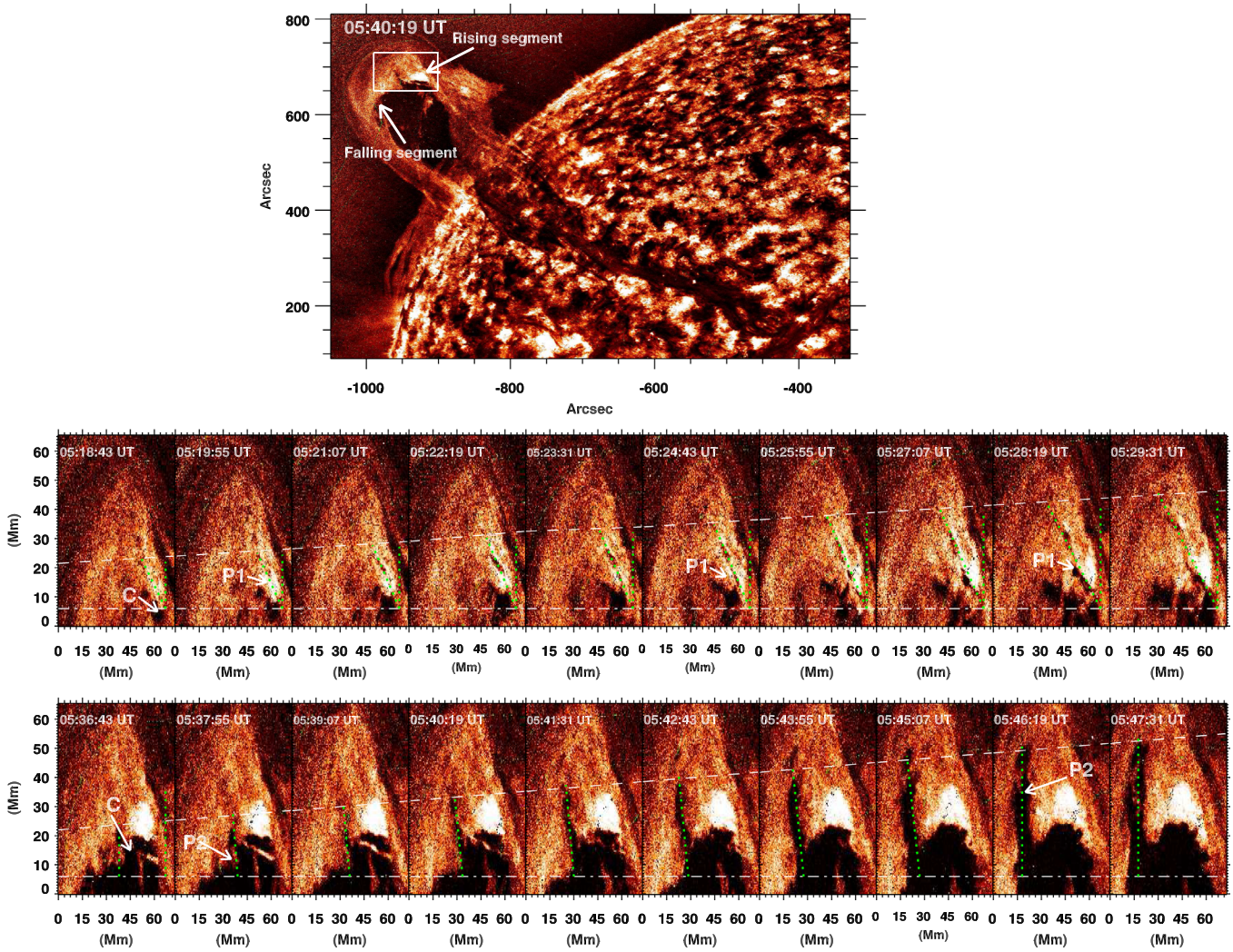

Figure 1. Upper panel: the full FOV of the loop-like prominence observed by *SDO*/AIA 304 Å on 2014 November 18th after applying multi-Gaussian normalized filter. The sub-region (white box) consists of an MRT-unstable plume. Middle panel: a dark cavity has been evident within the prominence. The spatiotemporal evolution of MRT-unstable plume (P1) has been observed. Lower panel: the second plume, "P2," is tracked at different heights and times to estimate the observational growth rate of the MRT instability. The temporal image data in the middle and lower panels show the increments in time from right to left. This is the partial FOV of an eruptive prominence where all plasma processes related to MRT instability are evolved.

where n is the number density, EM is the total emission coming from the different temperature bins, and "l" is the depth of the region from which the emission occurred. The filling factor for the density estimation into the flux rope is assumed to be 1. We assume that the width of the prominence at the prominence–cavity interface is equal to the depth of the prominence (Cheng et al. 2012a, 2012b). The estimated mass density is used for the evaluation of the magnetic field and theoretical growth rate of the MRT instability.

Using the abovementioned observational data and various analysis techniques, we have observed a prominence that was at equilibrium for more than three days. The prominence started to grow around 04:30 UT and erupted at 07:38 UT on 2014 November 18th. During the rising phase of this prominence, it exhibited the evolution of magnetic Rayleigh–Taylor unstable plumes in its upper part. A cavity developed within the overlying prominence at 05:15 UT, acting as an initial perturbation. As the perturbation grew, it initiated the development of the first MRT-unstable plume (P1; Figures 1–2). Ryutova et al. (2010) set the criteria for the observed plumes to be Rayleigh–Taylor unstable. These criteria are multi-mode front, self-similarity, and suppression of the regular oscillations of the prominence. We observe the two modes of plumes (P1 and P2), which show the similarities in the wavelength/width ratio. Strong upflow is observed in the overlying prominence. These additional perturbations pass through the prominence–cavity interface, which initiates a single-mode MRT-unstable plume (P2) at 05:36 UT (Figure 1, bottom panel). The self-similar plume formation (P1 and P2) shows the linear phase, and in a later stage the single-mode plume formation (P2) exhibits the nonlinear phase of MRT instability as it is converted into a mushroom-like structure in its final stage of development. The spatiotemporal evolution of MRT-unstable plumes is shown in Figure 1. The MRT instability is destroyed by the shearing and downfall in the prominence–cavity interface. Small-scale vortex-like structures have formed at the interface of the downfalling plasma and cavity (Figure 3). These vortex formations indicate that the MRT-unstable plume structures may be converted into Kelvin–

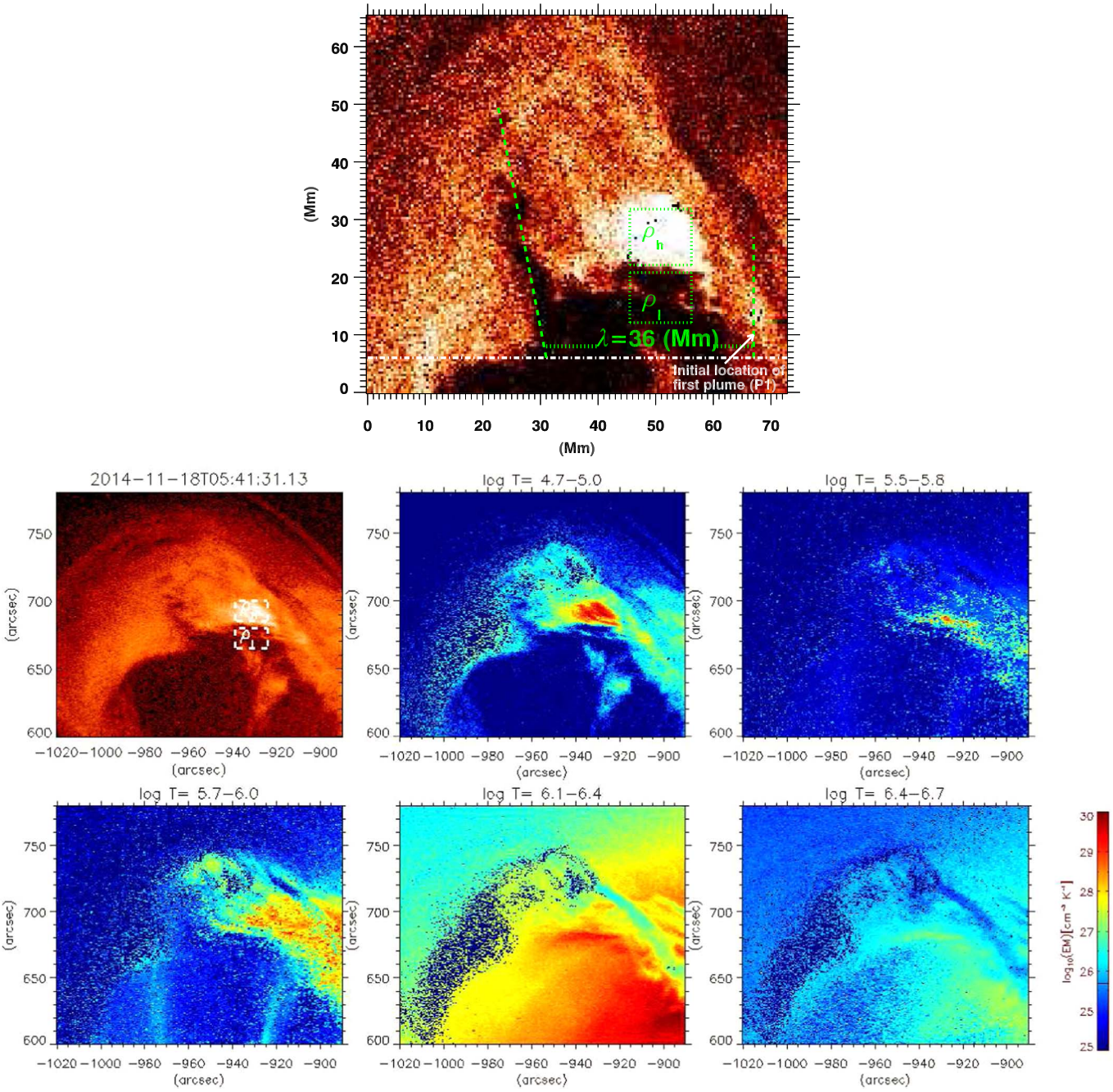

Figure 2. Upper panel: the sub-region of the eruptive prominence using a multi-Gaussian normalized filter on an AIA 304 Å image. A vertical line is drawn to indicate the initial location of the first plume (P1). The separation between the two consecutive plumes is the characteristic wavelength of an MRT instability. Lower panel: DEM of the same sub-region to observe the thermal structure of this MRT-unstable prominence.

Helmholtz instability and show the nonlinear phase of an MRT instability. A detailed interpretation is outlined in the subsequent subsection.

We observed that in the rising plasma segment, a tangled plasma thread passes through the overlying prominence at 06:43 UT (Figure 4). The tangled vertical thread is associated with Rayleigh–Taylor instability (van Ballegooijen & Cranmer 2010). The tangled thread passes into the overlying prominence with velocity $\approx$220 km s^{-1}. In the tangled thread, the bright location indicates a dip (Figure 4). The thickness of the thread is observed as $\approx$3.5 Mm. As it passes through the overlying prominence, a cavity develops along the length of the thread and later it is responsible for the shearing into the thread-like structures (Figures 5–7). Due to shearing motion at the interface, small-scale vortex-like structures move along the thread with a lifetime of 150–200 s. These vortex-like structures possibly formed due to the Kelvin–Helmholtz instability at the interface of the prominence and cavity. Later, more than five plasma blobs were observed at the same interface (Figure 8). These silent features of the observed highly localized plasma processes (i.e., plumes, thread, blobs) in different evolutionary stages of an eruptive prominence are explained, along with their theoretical interpretation, in Sections 3–4.

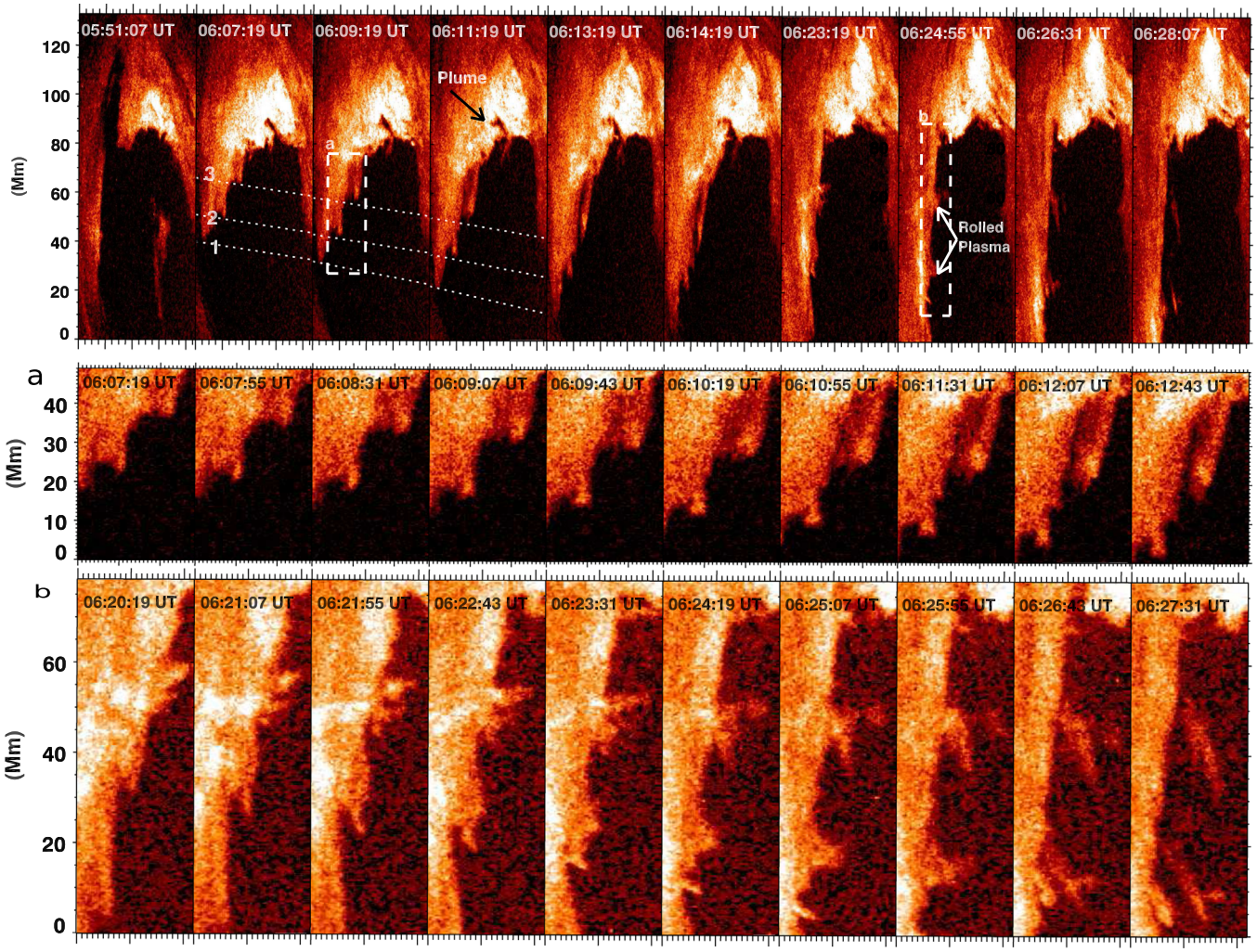

Figure 3. Top panel: the spatiotemporal variation of the full FOV of the overlying prominence, which collapses by plasma downfall. The white boxes "a" and "b" indicate the region where KH unstable vortices and rolled plasma structures are formed. The evolutions of these vortices and rolled plasma structures are shown in the lower panels. The online animation shows the plasma dynamics during the downfall. It runs from 05:50 to 06:34 UT, and includes annotations of the locations of plumes, perturbations, vortices, and rolled plasma structures.

(An animation of this figure is available.)

3. Observational Results

3.1. Formation of MRT-unstable Plumes

As abbreviated above, we observed a loop-like prominence eruption on 2014 November 18th during 04:00 UT to 07:50 UT with *SDO*. Before going to the eruptive stage, this quiescent prominence remained in the stable state for more than three days. We used the high-resolution and high-cadence multi-wavelength data (94, 131, 171, 193, 211, 304, 335 Å) of AIA (Lemen et al. 2012) to observe the dynamics of the magnetic Rayleigh–Taylor unstable plumes and plasma threads. Prominence plumes are dark structures in the cool temperature filters of AIA and they appeared bright in the form of hot structures at comparatively high temperature filters. The plume-like structure is generated from the large-scale cavity or bubbles that evolved within the prominence. They pass through the overlying prominence before they get fragmented. The plumes and plasma bubbles were first observed by Stellmacher & Wiehr (1973) and later it was hypothesized that these plumes were generated due to the magnetic Rayleigh–Taylor instability (Ryutova et al. 2010). We observed a loop-like prominence that consists of MRT-unstable plume-like developments in its upper part (Figure 1). We saw that the small-scale bubbles started to grow on 2014 November 18th after 05:00 UT. The source of these bubbles is not clear. Initially, these bubbles developed in the horizontal and vertical directions. Small-scale perturbations developed at the boundary of the cavity and overlying prominence. We observed that some of these perturbations further developed on a small spatial scale. One of the perturbations becomes unstable at 05:15 UT and passes through the overlying prominence with dark upflows (Figure 1). The magnetic Rayleigh–Taylor instability appeared when a contact of discontinuity formed along the magnetic interface, where a denser fluid lies over a less dense fluid and accelerates against the gravity. We observed that the cavity and the dark upflows generated within the overlying prominence are in the temperature range of (6.3–12.5) $\times$ 10^5 K, which is 12–25 times hotter than the surrounding prominence plasma (Figure 2). The hotter plasma lies below the cooler plasma and hence it may be the source of the buoyancy. Due to the buoyancy force, the dark plume=like structures are lifted up with the vertical upflows. The interface of the prominence–

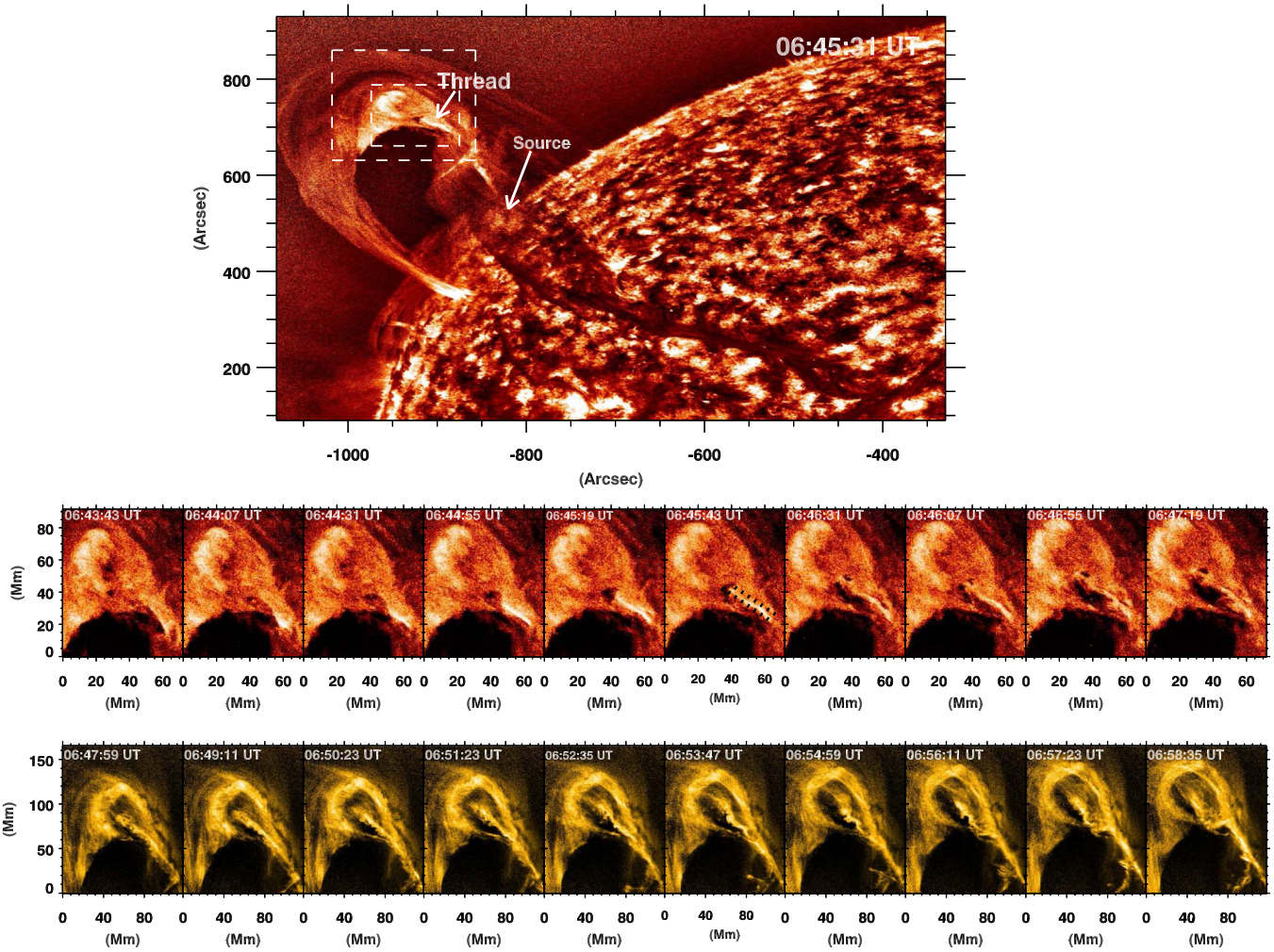

Figure 4. Top panel: full FOV of a multi-Gaussian normalized and fitted *SDO*/AIA 304 Å filter, which consists of a Rayleigh–Taylor unstable prominence thread. Middle panel: the sequence of images of the sub-region in the *SDO*/AIA 304 filter showing the temporal evolution of the plasma thread. Lower panel: the V-shaped dip as seen in the lower panel in the *SDO*/AIA 171 Å filter.

cavity system supports the magnetothermal convection in the solar atmosphere (Berger et al. 2011). The bright and denser region is associated with the overlying prominence and the dark and less denser cavity is associated with the ambient coronal plasma (Figure 2). The denser plume and prominence regions lie at different temperatures, therefore they are magnetically insulated because thermal conduction in the corona occurs along the field lines (Innes et al. 2012; Priest 2014). A magnetic interface is presented between the hot plume and cool prominence region. The density gradient works toward the Sun center following the direction of gravity. The magnetic tension component of the Lorentz force may accelerate the dark plumes against the gravity and density gradient. Therefore, the dark plumes satisfied the criteria of magnetic Rayleigh–Taylor instability. The lifetime of the dark plume (P1) is ≈14 minutes and it propagates with a constant velocity of $\approx 35\,\mathrm{km\,s^{-1}}$ in the overlying region before it is fragmented (Figure 1, middle panel). The width of the plume (P1) lies between 3 and 7 Mm (Figure 1). The main characteristic of the magnetic Rayleigh–Taylor instability is that the formation of multiple self-similar plumes occurs in its linear phase (Ryutova et al. 2010).

The cavity grows and it takes on a semi-spherical shape (Figure 1, bottom panel). Additional perturbations develop at the cavity-prominence interface, which further triggers the second plume (P2; Figure 1, bottom panel). We observed that this plume also satisfies the MRT instability criteria. The development of the second plume (P2) indicates the transformation from the linear phase to the nonlinear phase of MRT instability. We observe that the plumes has vertical upflows in the linear regime of MRT instability during 05:36 UT to 05:43 UT. At the boundary of the second plume (P2), regular dark and bright oscillatory patterns are presented. These regular oscillatory patterns indicate that the multiple self-similar RT unstable plumes may have evolved. After 05:43 UT, we observed that the interface of the dark plume (P2) and prominence became smooth and it may have shown the quasilinear phase of MRT instability. After 05:46 UT, it transforms into a single-mode plume and exhibits the nonlinear phase of MRT instability. We observe that this plume takes the shape of a mushroom cap structure in its final stage of development before entering the stable mode (Figure 1, bottom panel). The nonlinear explosive phase of the Kelvin–Helmholtz instability and the mushroom-like structures via nonlinear MRT instability are characterized by the single-mode plume formation (Ryutova et al. 2010). Therefore, the final stage of the plume (P2) formation exhibits the nonlinear phase of the instability in which the single-mode plume dominates by

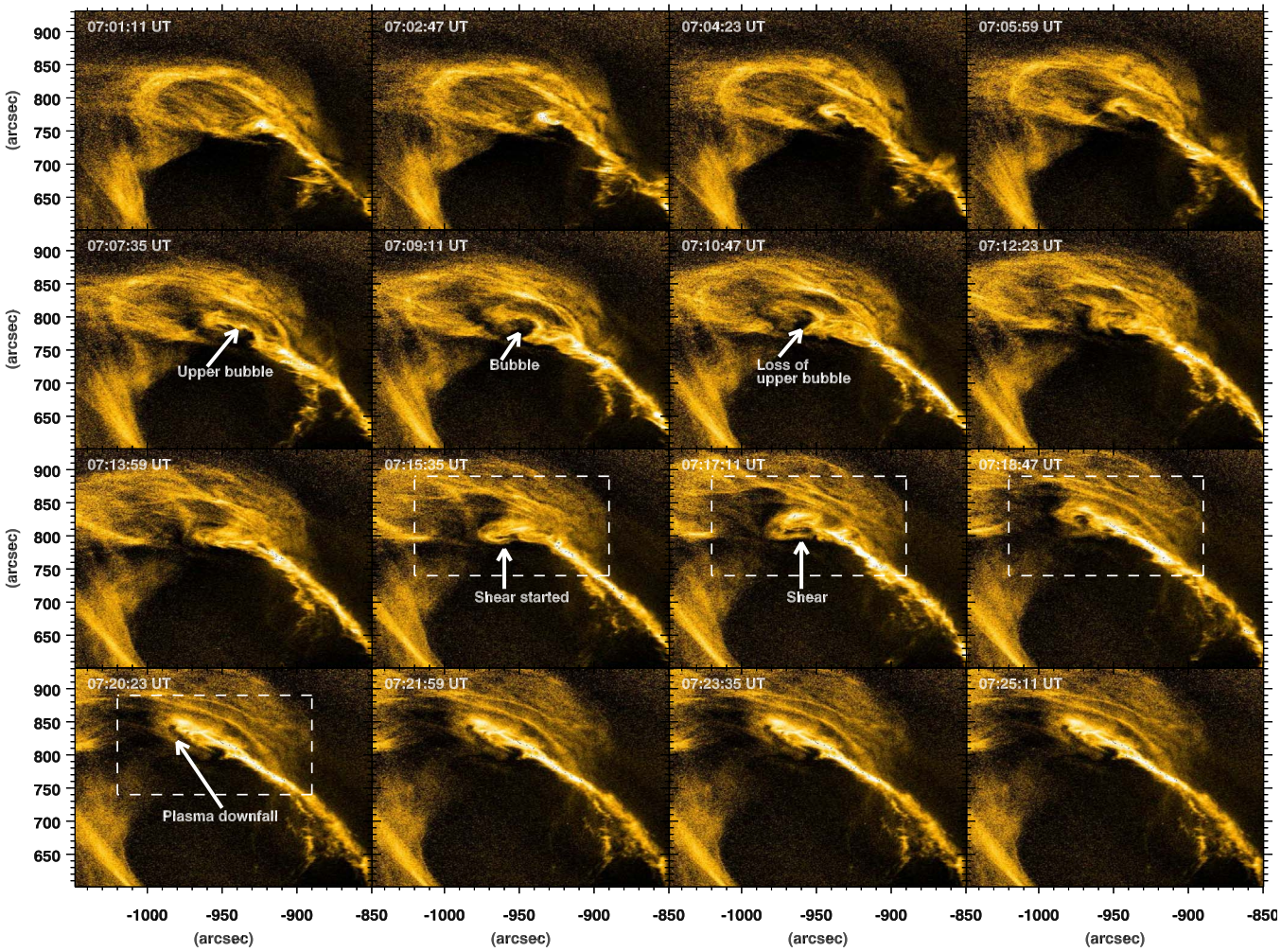

Figure 5. The sequence of images of *SDO*/AIA 171 Å shows the prominence–cavity boundary, which became unstable. The middle panel shows that two bigger plasma bubbles are observed. Later they may be responsible for the shear motion at the interface. The shear motion initiates the Kelvin–Helmholtz unstable vortex formation and Rayleigh–Taylor unstable bubbles are also formed at the boundary.

producing mushroom cap-like structures (Figure 1, lower panel). The lifetime, width, and upflow velocity of the single-mode plume are greater than those of the multi-mode plume formation. We have observed that the lifetime of P2 is greater than 40 minutes, and the maximum width is 14–16 Mm. It grows with the constant upflow velocity of $49\,\mathrm{km\,s^{-1}}$ (Figure 1).

3.2. Estimation of Theoretical and Observational Growth Rates of MRT-unstable Plumes

We identify two MRT-unstable plumes (P1 and P2) that propagate in the form of dark upflows into the overlying prominence with velocities of ∼35 and ∼49 $\mathrm{km\,s^{-1}}$, respectively. We observe the spatial and temporal evolution of the MRT-unstable plumes (Figure 1). The growth rate of the MRT instability during its linear and quasilinear phases at height (h) and time (t) (Ryutova et al. 2010) is given by

$$\gamma_{\mathrm{Obs}} = \frac{1}{(t_2 - t_1)} \ln\left(\frac{h_2}{h_1}\right), \tag{2}$$

where h_1 and h_2 are the heights of the plumes at time t_1 and t_2. A well evolved plume first appeared on 2014 November 18th at 05:16 UT. We track the growth of the plume at a different height with time (Figure 1). The temporal and spatial evolution of the MRT-unstable plumes are observed for the estimation of the observational growth rate. The estimated observational growth rates of the two MRT-unstable plumes are listed in Table 1. The average value of the observational growth rate for plume (P1) is $1.32 \pm 0.29 \times 10^{-3}\,\mathrm{s^{-1}}$ and that for plume (P2) is $1.48 \pm 0.29 \times 10^{-3}\,\mathrm{s^{-1}}$. We observe that the observational growth rate for both the MRT-unstable plumes decreases incrementally with height.

We compare the observational growth rate of the MRT-unstable plumes with the theoretical growth rate of the MRT instability. If γ_{th} is the theoretical growth rate of the MRT instability, ρ_h and ρ_l indicates the mass density within the bright dense region (plumes here) and dark cavity region, respectively, at the prominence–cavity interface, the linear stability theory (Chandrasekhar 1961; Ryutova et al. 2010; Priest 2014) describes the growth rate of the MRT instability as

$$\gamma_{\mathrm{th}} = \sqrt{\frac{2\pi g}{\lambda} A\left[1 - \frac{B^2 \cos^2\theta}{(\rho_h - \rho_l) g \lambda}\right]}, \tag{3}$$

where g is the acceleration due to the gravity of the Sun, B is the horizontal component of the magnetic field, λ is the

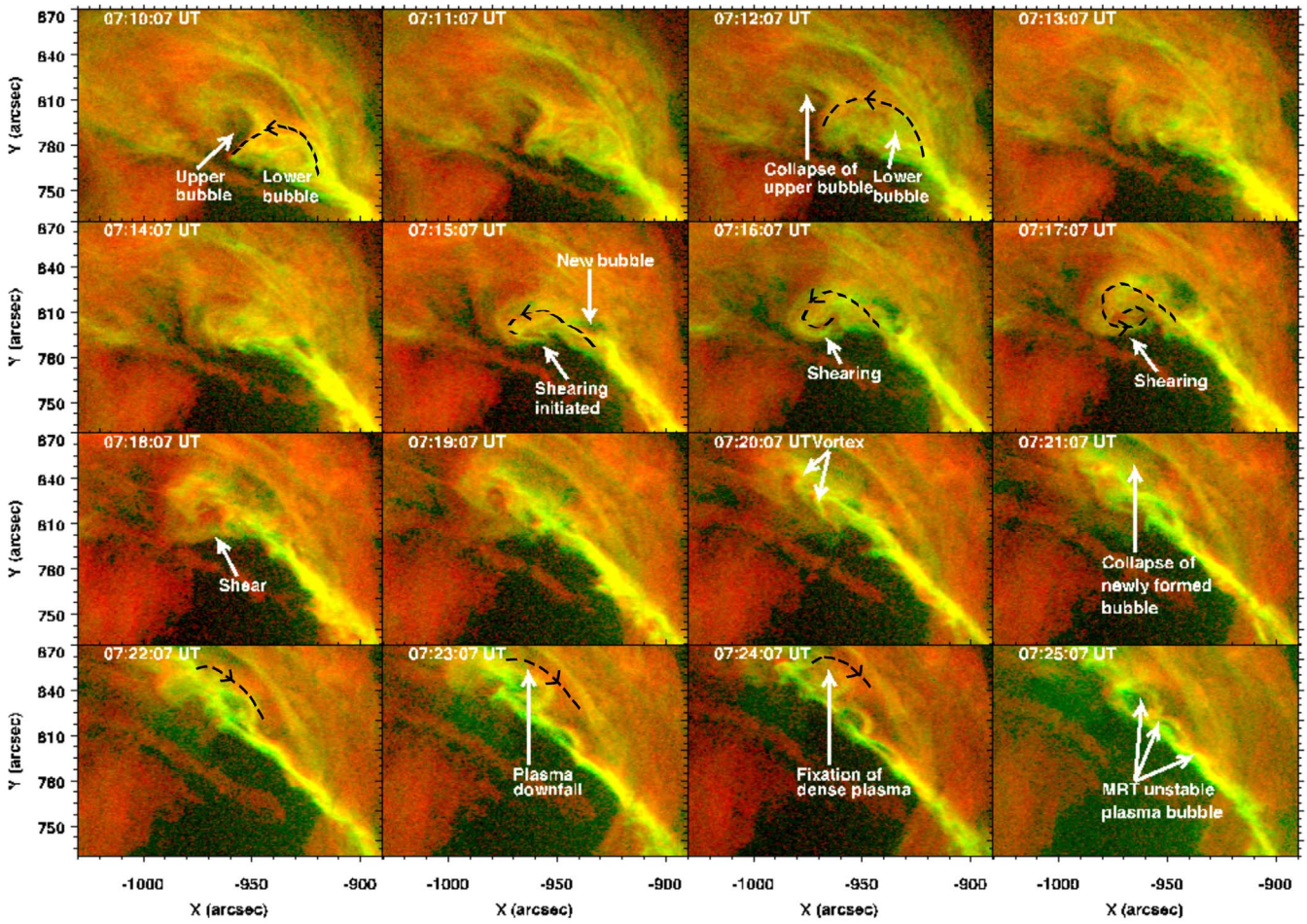

Figure 6. The region of interest (ROI; white box in Figure 5) is displayed in the *SDO*/AIA (171 + 304) Å composite images. The composite images observed the characteristics of the bubble–prominence boundary. Shear motion, plasma downfall, MRT-unstable bubbles associated with the Rayleigh–Taylor unstable thread are indicated by arrows at the interface. The animation of the *SDO*/AIA (171 + 304) Å composite images shows the complete evolution of shearing, bubble formation, MRT-unstable bubbles, and the collapse of the bubbles at the prominence–cavity interface; it runs from 07:00 to 07:34 UT. The white arrows annotate features in the animated version.

(An animation of this figure is available.)

characteristic wavelength of the MRT instability, A is Atwood number which is given by $A = \frac{\rho_h - \rho_l}{\rho_h + \rho_l}$, and θ is the angle between the magnetic field (B) and wave vector of the MRT-unstable perturbations. The magnetic field component of the growth suppresses the instability. Therefore, we can say that as the plumes pass through the higher height, the magnetic field component reduces the growth of MRT instability. We observe that the theoretical growth rate contains all the measurable parameters.

We adopt the sparse inversion code to estimate the mass densities within the plume regions and below the dark coronal region (Cheung et al. 2015). The width of the prominence at the prominence–cavity interface is ∼75 Mm. The total emission measures (EMs) coming from the bright region and dark cavity region are 3.2×10^{29} cm^{-5} and 1.4×10^{29} cm^{-5}, respectively, along the prominence body. The plasma densities $\left(n = \sqrt{\frac{\mathrm{EM}}{l}}\right)$ associated with these two regions have been estimated as 6.5×10^{9} cm^{-3} and 4.3×10^{9} cm^{-3}, respectively. The assumed composition of the prominence is 45% H°, 45% H^+, 9% He°, 1% He^+ (Labrosse et al. 2010; Gilbert et al. 2011). The estimated mass densities for the bright dense region ρ_h and the dark cavity region ρ_l are 1.4×10^{-14} and 9.3×10^{-15} gm cm^{-3}, respectively (Figure 2). An updated version of the sparse inversion code is "sparse code new," which is useful to measure the total emission of the hotter plasma (Su et al. 2018). This new updated version introduced the sparse inversion code and mapped the thermal plasma from ∼0.3 to ∼30 MK. It is important, particularly for flare initiation, current sheets, cusps, super-arcade downflows, shocks, active regions, EIT waves, etc. In the present case, we observe that most of the emissions are coming from the lower temperature (304 Å) for the prominence. The emission from the 304 Å filter is optically thick and has high opacity compared to the other six filters of *SDO*/AIA. The higher opacity may be the cause of the saturation of the continuum absorptions, therefore slight underestimation of the mass density may be observed (Heinzel et al. 2008; Gilbert et al. 2011). In the given observational baseline, we therefore utilize the method of Cheung et al. (2015), which gives results that are almost consistent with those derived following Su et al. (2018).

From Equation (3), when $\theta = 0$, i.e., for the condition where the magnetic field is oriented in the same direction for the dense

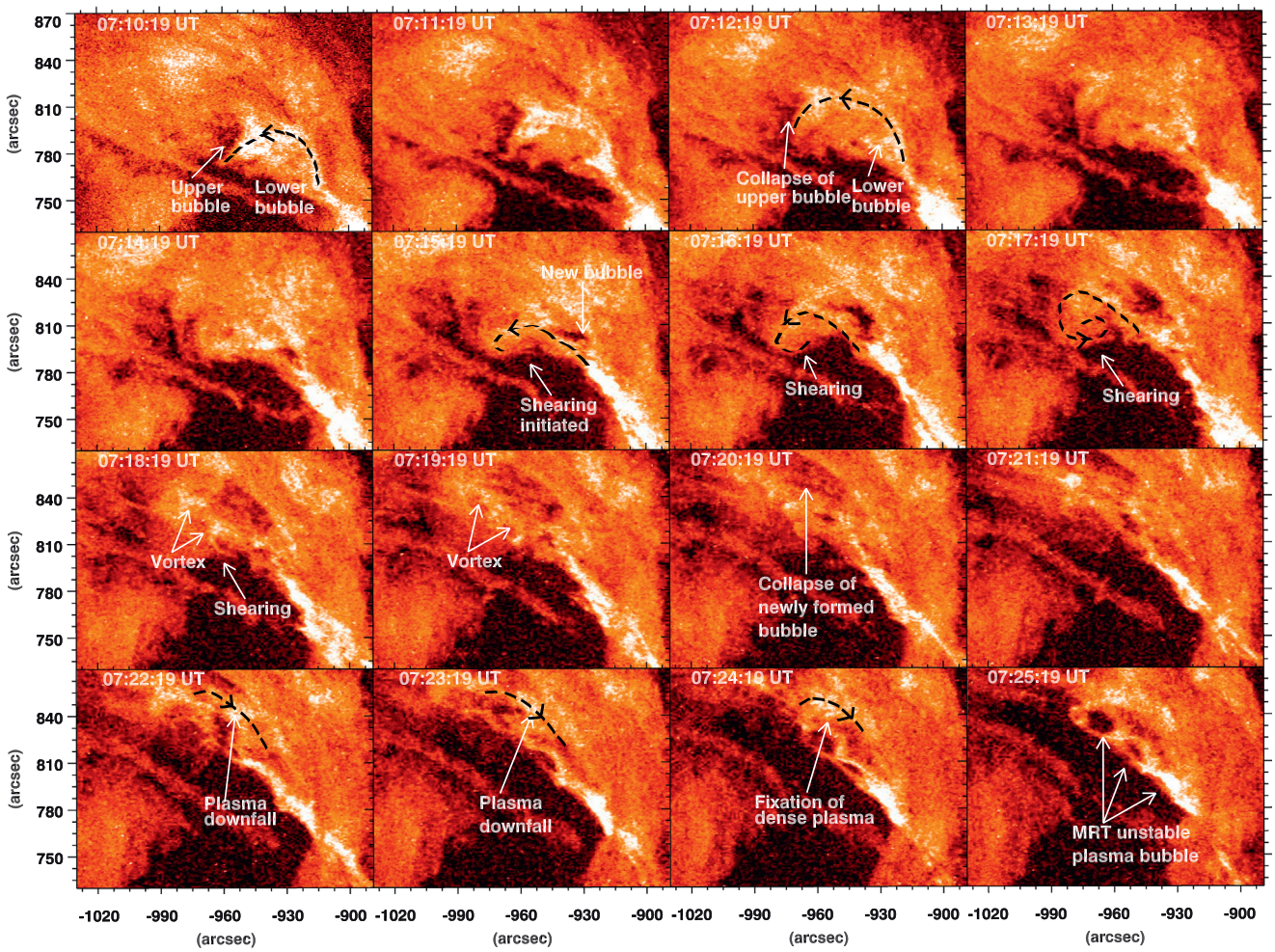

Figure 7. The region of interest (ROI; white box in Figure 5) is displayed using *SDO*/AIA 304 Å images. MRT-unstable bubbles, shear motion, and a KH unstable vortex are indicated by arrows at different time epochs of the prominence–cavity boundary. The animation of the *SDO*/AIA 304 Å images shows the complete behavior of the prominence–cavity boundary and different morphological structures; it runs from 07:06 to 07:33 UT. The white arrows annotate features in the animated version.

(An animation of this figure is available.)

region and the less dense region, the maximum growth rate could be attained (Chandrasekhar 1961; Ryutova et al. 2010; Priest 2014). Therefore, for the maximum growth rate, $\gamma_{\rm th} = 0$,

$$-gk\frac{(\rho_h - \rho_l)}{(\rho_h + \rho_l)} + \frac{B^2k^2\cos^2\theta}{2\pi(\rho_h + \rho_l)} = 0, \quad (4)$$

where k is the wave vector associated with MRT instability. The instability occurred when $k < k_c$, which is related to the critical wavelength λ_c. The critical magnetic field (B_c) is given by

$$B^2 = g\lambda_c(\rho_h - \rho_l). \quad (5)$$

We observe that the bright and denser regions are heavier than the less dense and dark regions, so we take $\frac{\rho_h}{\rho_l} > 1$. The Alfvén velocity for the rising MRT-unstable plume is (Innes et al. 2012)

$$B^2 = 4\pi\rho_h V_A^2. \quad (6)$$

Therefore we obtain:

$$V_A = \sqrt{\frac{\lambda_c g}{4\pi}}. \quad (7)$$

The separation between two consecutive MRT-unstable plumes (Figure 2) gives the characteristic wavelength $\lambda = 36$ Mm. Analogous to this wavelength, the Alfvén velocity (V_A) is $\approx$28 km s^{-1}. We have estimated the magnetic field (B) $\approx$ 1.32 G. Therefore, to estimate the theoretical growth rate, we take $\rho_h = 1.43 \times 10^{-14}$ gm cm^{-3}, $\rho_l = 9.32 \times 10^{-15}$ gm cm^{-3}, Atwood number (A) = 0.21, solar gravity (g) = 274 m s^{-2}, and characteristic wavelength (λ) = 36 Mm. We observed that the first plume propagates at an angle $\theta_1 = 48°$. For the second plume (P2), θ_2 is 82° from the top of the cavity, where the plume originates in the projected plane. The theoretical growth rate of the MRT instability is estimated as $\gamma_{\rm th} = 1.95 \times 10^{-3}$ s^{-1}, which is in good agreement with the observed growth rate (Table 1).

We observe that after the full development of the second MRT-unstable plume (P2), the downfall begins in the falling segment. The full growth of the plume (P2) occurred at 05:50 UT, where it gained the mushroom cap-like structure

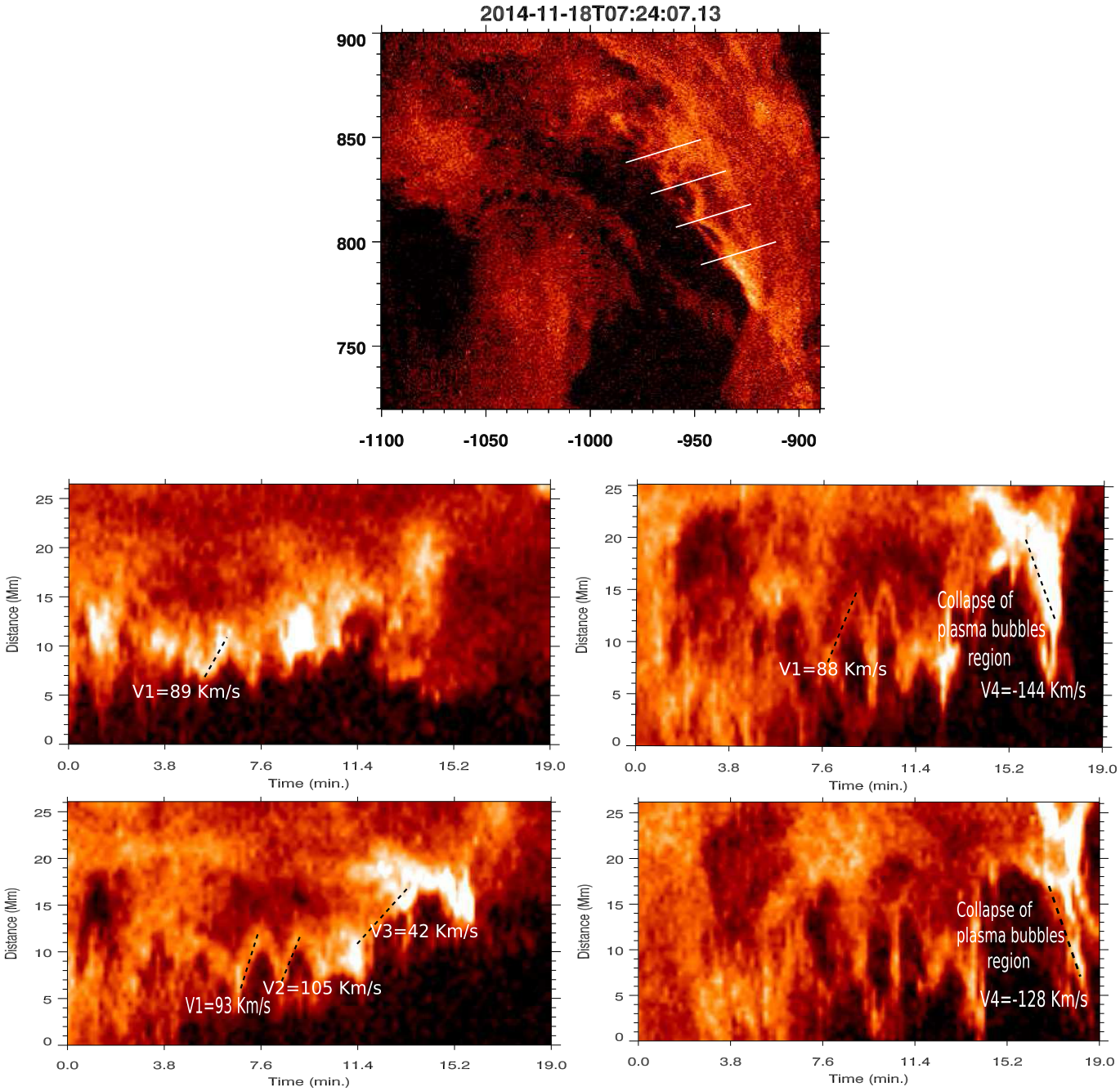

Figure 8. MRT-unstable prominence bubbles are tracked at different heights at the prominence–cavity interface. The observed bubbles propagate with different velocities and attempt to merge within themselves. The collapse phase of MRT-unstable bubbles is shown in the lower panel.

(Figure 3). The MRT-unstable plumes try to attain stability. Time-sequence images aren used to study the spatial variation of the downfalling plasma (Figure 3, top panel). The additional perturbations continuously developed at the interface of the prominence and cavity. To achieve stability, the loop-like prominence releases the shear at the prominence–cavity interface (Figure 3). After 06:03 UT, some of the perturbations developed nonlinearly and converted into an MRT-unstable plume and some rolled-up structures at the prominence–cavity boundary (Figure 3, boxes "a" and "b"). At the boundary of the falling plasma and cavity, three small-scale rolled-up plasma substructures are observed (see also the animated version of Figure 3). These rolled substructures formed at regular intervals. The velocities of the leading edge of the downfalling plasma and two rolled-up structures that are marked 1, 2, and 3 are 70, 58, and 55 km s^{-1}, respectively. It should be noted that under the given spatial resolution and emissions of AIA 304 Å, the fine structures related to the rolling in these vortices are observed. It is clear in Figure 3 and its animation that the central bright cores within these small-scale structures are rolling and comparatively less intense plasma around the core is trying to envelop and bend (see panels "a" and "b", of the Figure 3 animation). However, we wish to point out that this is more a qualitative description based on the obtained 304 Å images as observed by AIA. We need more high-resolution observations to resolve the fine structured vortex motions at the prominence–cavity interface. Later, few rolled plasma structures are observed at the prominence–cavity interface (Figure 3,

Table 1
Projected Height Estimation of the Plumes (P1 and P2) w.r.t. Normalized Height

Projected Height (Mm) of the Plume (P1) with Respect to Position of the Cavity "C"	Projected Height (Mm) of the Plume (P2) with Respect to Position of the Cavity "C"	Time Interval (t_2–t_1)	Observed Growth Rate for the Plume (P1) $\gamma_{\rm Obs1} = \frac{1}{(t_2-t_1)} \ln\left(\frac{h_2}{h_1}\right) \times 10^{-3}\ {\rm s}^{-1}$	Observed Growth Rate for the Plume (P2) $\gamma_{\rm Obs2} = \frac{1}{(t_2-t_1)} \ln\left(\frac{h_2}{h_1}\right) \times 10^{-3}\ {\rm s}^{-1}$
16.5	18.3	0	0	0
19.0	21.6	72	1.96 ± 0.29	2.30 ± 0.29
21.5	24.9	72	1.72 ± 0.21	1.97 ± 0.20
24.0	28.1	72	1.53 ± 0.16	1.68 ± 0.15
26.5	31.4	72	1.38 ± 0.13	1.54 ± 0.11
29.0	34.7	72	1.25 ± 0.10	1.39 ± 0.09
31.5	38.0	72	1.15 ± 0.08	1.26 ± 0.07
34.0	41.3	72	1.06 ± 0.07	1.16 ± 0.06
36.5	44.6	72	0.98 ± 0.06	1.06 ± 0.05
39.0	47.9	72	0.92 ± 0.05	0.99 ± 0.04

Note. The normalized height is considered with respect to the position of cavity "C" situated 471 Mm from the Sun's center. The observational growth rate of MRT instability is estimated by tracking the height of the observed plumes at different times.

lower panel). These plasma structures may have formed due to Kelvin–Helmholtz instability. Therefore, we conjecture that the MRT-unstable plumes attain stability through Kelvin–Helmholtz vortex formation. The animation for Figure 3 shows the observed rolled-up structures and related plasma dynamics.

4. Formation of Tangled Threads and Plasma Bubbles Due to the Hybrid KH-MRT Instability

4.1. Tangled Threads

After one hour of the evolution of MRT-unstable plumes, a thin bright thread was observed in the rising segment of the loop-like prominence. The thread first appeared on 2014 November 18th at 06:44 UT (Figure 4). The main source of the thread is not clear on the solar disk, because the lower part of the prominence is partially covered by the eruption site. The typical lifetime for the thread is 8–10 minutes, with a maximum thickness of 3.5 Mm (Figure 4, middle panel). A dark cavity region was observed between the top of the thread and the overlying prominence. The thread drags the cavity region and is trapped within the overlying prominence (Figure 4, middle panel). A random orientation of field lines and V-shaped structures is observed at the prominence–cavity interface (Figure 4, bottom panel). The prominences are supported by the pressure of the sheared magnetic field. It acts as the tenuous fluid region and shows its buoyant nature. If a tenuous fluid supported the denser fluid against the gravity it becomes Rayleigh–Taylor unstable (Chandrasekhar 1961). The observed thread satisfies similar constraints and may be subjected to Rayleigh–Taylor instability (van Ballegooijen & Cranmer 2010). The cool plasma is collected into the dip regions of the tangled field. The temporal and spatial evolution of the tangled plasma thread is displayed in Figure 4.

4.2. Evolution of the Hybrid KH-RT Instability

In this section, we discuss the possibility of hybrid Kelvin–Helmholtz & Rayleigh–Taylor (KH-RT) instability at the prominence–cavity interface. We observe that as the tangled plasma thread passes through the overlying prominence, small-scale bubbles develop between the thread and surrounding prominence. The loop-like prominence eruption is triggered by an instability that is associated with the shear on the prominence–cavity interface (see Figures 6 and 7 and , and the associated animations). The shear that develops at the interface is diffused and rapid, therefore analyzing the shear and instability is very difficult. In these observations optical flow measurements like local correlation tracking, differential affine velocity estimator, and nonlinear affine velocity estimator are not likely to be useful for understanding the fine structures, as the shearing developed far off the limb (Chae & Sakurai 2008). In this section, we do not perform any quantitative analysis, but we observe the shear qualitatively by analyzing the time-series of the imaging observations.

The thread-like structures appear on 2014 November 18th at 06:43 UT and interact with a leg (northward lying) of the overlying prominence (Figure 4). Two eruption sites are observed that continuously erupt the plasma along the thread and these plasmas interact with the one leg of the overlying prominence. The eruption sites are not clearly observed on the solar disk, as they are partially covered by the prominence leg. The observed plasma thread is trapped in the upper loop-like prominence and larger cavity region. The tangled thread has a dip region that is observed as V-shaped structures containing more prominence plasma. The loop-like prominence and thread consist of a tangled magnetic field. Due to the relative motion of these two, the field lines stretch in the vertical direction. Therefore, the shear increases with time at the prominence–cavity interface (Figures 5–7, and the associated animations). The spatial dynamics of the cavity-prominence boundary are observed using the time-sequence images (Figures 5–7, and the associated animations). We observe that a new cavity/bubble developed at the prominence–cavity interface after 07:07 UT. This cavity was dragged by the dense plasma material, which linked with the two eruption sites and was trapped between the thread and overlying prominence. The dense region coming from the eruption site fills the cavity and it may change the structure of the cavity when it interacts with the overlying thread and prominence. The observed cavity region is associated with the low dense and hotter plasma materials and an excess of emission around 1 MK in the corona (Berger et al. 2011; Hillier 2018). They are surrounded by cooler and denser prominence plasma (Figure 6, and the animated versions of Figures 6 and 7). The hotter and less dense plasma lies below the cooler and denser prominence plasma and hence it

may act as the source of the observed buoyancy and density inversion. Therefore, the observed plasma bubbles are magnetic Rayleigh–Taylor unstable at the prominence–cavity interface. After 07:10 UT, we observe a complex configuration forthe prominence–cavity interface and a collapse of the cavity at the same interface. The collapse of the cavity may trigger the shear flows at the interface. To observe the shear flow qualitatively, we selected a region of interest (dotted white box in the bottom panel of Figure 5). The shear flow is very diffused and rapid, therefore we use the array of images with durations of 15 minutes and 60 s cadences. The shear flow collapses after few a minutes from the plasma downflow near the prominence–cavity boundary. The plasma downflow and shear flows may trigger the instability at the cavity-prominence boundary. The shear flow fixes the denser plasma at the top of the thread and small-scale plasma bubbles form at the boundary of the prominence and cavity. We track these plasma bubbles at different heights and times by taking the slits at different heights (Figure 8, top panel). We observed that MRT-unstable plasma bubbles grew with time and had a regular oscillatory pattern with an approximate period of 124 ± 18 s (Figure 8, middle and lower panels). An oscillatory pattern at the interface may indicate bumps of plasma at the interface. These bumps possibly developed due to Kelvin–Helmholtz instability caused by shear flow at the prominence–cavity interface. The observed plasma bubbles are magnetic, Rayleigh–Taylor unstable, and Kelvin–Helmholtz unstable simultaneously at the interface. Therefore, we discussed the possibility of hybrid KH-RT instability at the prominence–cavity interface. Some theoretical works have examined coupled KH-RT instability (e.g., Zhang et al. 2005; Olson et al. 2011; Ye et al. 2011). Berger et al. (2017) used *HINODE*/SOT data to observe the dynamics of the prominence–cavity boundary. They reported that the quiescent prominence–cavity interface dynamics shows the evolution of the coupled KH-RT instability; this was the first observational proof of hybrid KH-RT instability.

The different plasma bubbles move with different speeds on the interface. In the upper part of the eruption, shearing starts due to the relative motion of the erupted plasma and overlying prominence. Due to their relative motions and different plasma bubble velocities, internal mergers begin (Figure 8). We have estimated the theoretical merging time for these plasma bubbles using (Ryutova et al. 2010)

$$\tau_{\rm th} = \frac{\Delta U}{0.1Ag}, \tag{8}$$

where "ΔU" is the velocity difference between two consecutive bubbles, "A" is Atwood number, and "g" is the acceleration due to gravity. The density within the bright plasma blobs is $(\rho_h) = 1.65 \times 10^{-14}\,\mathrm{gm\,cm^{-3}}$. In the dark region $(\rho_l) = 0.92 \times 10^{-14}\,\mathrm{gm\,cm^{-3}}$. These densities have been estimated by measuring the total emissions (Cheung et al. 2015). Using the measured velocity difference $\Delta U = 12\,\mathrm{km\,s^{-1}}$, and Atwood number $(A) = 0.29$, we get the theoretical merging time $(\tau_{\rm th}) = 24$ minutes 30 s. The observational merging time is approximately 17 minutes 40 s, which is illustrated in Figure 8. The theoretical merging time is reasonably comparable to the observational merging time of the plasma bubbles.

The perturbations from the two eruption sites and the associated shear flow may be the main cause of hybrid KH-RT instability. During the growth of this instability, the overlying prominence also becomes unstable. As the merging of the plasma blobs was completed, the overlying prominence became unstable and erupted toward the outer corona. Therefore, we could assume that the hybrid KH-RT instability may be the main cause of the eruption of the overlying prominence and the generation of the associated CME. The lower segment of the prominence thread consists of the bulky plasma material, which is further observed in the outer corona in the form of plasma blobs.

5. Discussion and Conclusions

A loop-like quiescent prominence erupted on 2014 November 18th at 07:30 UT. Before the eruption, the prominence remained in the stable state for more than three days and one leg was covered with one-fourth of a solar disk. In the present paper, we observe the evolution of multi-mode magnetic Rayleigh–Taylor unstable plumes (P1 and P2) and their formation, which passes through the overlying prominence. Hybrid KH-RT instability at the prominence–cavity interface is also observed in the later phases.

In the upper part of the loop-like prominence, small-scale cavities appear and grow within the overlying prominence. After some vertical and horizontal growth of the cavity, some small-scale linear perturbations develop at the boundary of the cavity (Figures 1–2). A perturbation becomes nonlinear after 05:15 UT and forms a dark and hot plume (P1), which passes through the overlying prominence at an upflow speed of $\sim 35\,\mathrm{km\,s^{-1}}$. The DEM diagnostics show that the plume (dark upflow) is associated with the hotter and less dense coronal plasma as compared to the surrounding prominence. The higher density prominence region lies above the low-density dark cavity region, and they are supported against the gravity. Additional perturbations continuously grow at the boundary of the cavity. Another perturbation developed nonlinearly and converted into a larger MRT-unstable plume (P2). We estimate the observational growth rate of the MRT-unstable plumes (P1) and (P2) as $1.32 \pm 0.29 \times 10^{-3}$ and $1.48 \pm 0.29 \times 10^{-3}\,\mathrm{s^{-1}}$, respectively. We use the linear stability theory of MRT instability to estimate the theoretical growth rate of an MRT instability, which is found to be $1.95 \times 10^{-3}\,\mathrm{s^{-1}}$. It is in good agreement with the observational growth rate. The second plume (P2) is converted into mushroom cap-like structures in its final stage of evolution, which is characterized by a Kelvin–Helmholtz unstable single plume. The MRT-unstable plume collapses by the secondary Kelvin–Helmholtz instability, in which the two vortex-like structures and rolled plasma structures evolve in the plasma downfall at the boundary of the prominence–cavity (Figure 3). The secondary Kelvin–Helmholtz instability shows the nonlinear formulation of MRT instability. Therefore, we observe the full evolution of MRT-unstable plumes and their linear and nonlinear dynamics.

After the collapse of the MRT-unstable plumes (P1 and P2), the northward segment of the loop-like prominence consists of a bright plasma thread, which is evident at 06:43 UT in the overlying prominence (Figure 4). The plasma thread is associated with the tangled field and Rayleigh–Taylor instability, which may be responsible for the shearing motion at the prominence–cavity boundary. During the evolution of the plasma thread, plasma bubbles, shear motion, and plasma downfall are observed at the prominence–cavity interface (Figures 6, 7, and the associated animations). The plasma bubbles are trapped within the eruption site and overlying

prominence. The plasma bubbles may feel the depression due to the overlying prominence and may be responsible for the shear motion at that boundary. Falling plasma at the interface may increase the shear motion, which leads to the Kelvin–Helmholtz instability (Figures 5–7, and the animations associated with Figures 3 and 6). Later, the downfall of the plasma starts in the middle part of the plasma thread, which fixes the cool and dense plasma materials on the top of the thread at the interface. Due to the density inversion at the interface, MRT-unstable plasma bubbles are observed at the prominence–cavity boundary. The theoretical and observational merging times for these plasma bubbles are observed and they are consistent with each other. The shear flow at the prominence–cavity boundary may lead to the formation of a Kelvin–Helmholtz unstable vortex structure and MRT-unstable plasma bubbles at the same interface. Due to the hybrid KH-RT instability at the interface, the tangled magnetic field may try to balance the shear motion at the interface, which is sufficient for the collapse of MRT-unstable plasma bubbles.

In this paper, we have discussed the dynamics of MRT-unstable multi-mode plumes, which grew linearly and then converted into a single-mode plume, which indicates the nonlinear phase of MRT instability of the plume development in the loop-like prominence. Similar dynamics in MRT-unstable plumes were previously only reported hedgerow quiescent prominences (e.g., Berger et al. 2008, 2010, 2011; Ryutova et al. 2010; Hillier et al. 2011a, 2012a, 2012b; Hillier 2018). Ryutova et al. (2010) reported observational and theoretical growth rates in the quiescent prominence that were similar to what we observe in the case of an eruptive loop-like prominence. Later, we observed a prominence thread that may contain a tangled field and may be the cause of the shearing at the prominence–cavity interface. The thread-like structure is Rayleigh–Taylor unstable and may have created the shearing (van Ballegooijen & Cranmer 2010). Berger et al. (2017) analyzed the boundary of the hedgerow prominence–cavity boundary and reported the hybrid KH-RT instability for the first time. The interface at which the thread passes became unstable and showed characteristics of hybrid KH-RT instability. We observe similar hybrid KH-RT instability dynamics at the prominence–cavity interface in the case of a loop-like eruptive prominence.

The present work, to the best of our knowledge, provides the first proof of the development of MRT-unstable plumes and hybrid KH-RT instability together in a loop-like eruptive prominence. We find that these instability features develop on different spatiotemporal scales and in different regions of the prominence in a sequential manner. Therefore, they provide an overall scenario for the evolution of linear MRT instability, its conversion to the nonlinear phase, formation of the shear flows and vortices, and finally the generation of hybrid KH-RT instability phase.

We acknowledge the constructive comments of the referee, which improved the manuscript. A.K.S. and S.K.M. acknowledge the DST-SERB (YSS/2015/000621) project. A.K.S. acknowledges the UKIERI Research Grant for the support of his research. The authors acknowledge the use of the method developed by Mark Cheung (Cheung et al. 2015) to understand the thermal structure of the inner corona by observing the DEM. They also acknowledge the *SDO*/AIA observational data.

ORCID iDs

Sudheer K. Mishra https://orcid.org/0000-0003-2129-5728

References

Berger, T., Hillier, A., & Liu, W. 2017, ApJ, 850, 60
Berger, T., Testa, P., Hillier, A., et al. 2011, Natur, 472, 197
Berger, T. E., Shine, R. A., Slater, G. L., et al. 2008, ApJL, 676, L89
Berger, T. E., Slater, G., Hurlburt, N., et al. 2010, ApJ, 716, 1288
Carlyle, J., Williams, D. R., van Driel-Gesztelyi, L., et al. 2014, ApJ, 782, 87
Chae, J. 2010, ApJ, 714, 618
Chae, J., Ahn, K., Lim, E.-K., Choe, G. S., & Sakurai, T. 2008, ApJL, 689, L73
Chae, J., & Sakurai, T. 2008, ApJ, 689, 593
Chandrasekhar, S. 1961, Hydrodynamic and Hydromagnetic Stability (Oxford: Oxford Univ. Press)
Cheng, X., Zhang, J., Olmedo, O., et al. 2012a, ApJL, 745, L5
Cheng, X., Zhang, J., Saar, S. H., & Ding, M. D. 2012b, ApJ, 761, 62
Cheung, M. C. M., Boerner, P., Schrijver, C. J., et al. 2015, ApJ, 807, 143
de Toma, G., Casini, R., Burkepile, J. T., & Low, B. C. 2008, ApJL, 687, L123
Foullon, C., Verwichte, E., Nakariakov, V. M., Nykyri, K., & Farrugia, C. J. 2011, ApJL, 729, L8
Foullon, C., Verwichte, E., Nykyri, K., Aschwanden, M. J., & Hannah, I. G. 2013, ApJ, 767, 170
Gilbert, H., Kilper, G., Alexander, D., & Kucera, T. 2011, ApJ, 727, 25
Heinzel, P., Schmieder, B., Fárník, F., et al. 2008, ApJ, 686, 1383
Hillier, A. 2018, RvMPP, 2, 1
Hillier, A., Berger, T., Isobe, H., & Shibata, K. 2012a, ApJ, 746, 120
Hillier, A., Isobe, H., Shibata, K., & Berger, T. 2011a, ApJL, 736, L1
Hillier, A., Isobe, H., Shibata, K., & Berger, T. 2012b, ApJ, 756, 110
Hillier, A., Isobe, H., & Watanabe, H. 2011b, PASJ, 63, 19
Innes, D. E., Cameron, R. H., Fletcher, L., Inhester, B., & Solanki, S. K. 2012, A&A, 540, L10
Isobe, H., Miyagoshi, T., Shibata, K., & Yokoyama, T. 2005, Natur, 434, 478
Jun, B.-I., Norman, M. L., & Stone, J. M. 1995, ApJ, 453, 332
Labrosse, N., Heinzel, P., Vial, J.-C., et al. 2010, SSRv, 151, 243
Lemen, J. R., Title, A. M., Akin, D. J., et al. 2012, SoPh, 275, 17
Lin, Y., Engvold, O., Rouppe van der Voort, L., Wiik, J. E., & Berger, T. E. 2005, SoPh, 226, 239
Mishra, S. K., Singh, T., Kayshap, P., & Srivastava, A. K. 2018a, ApJ, 856, 86
Mishra, S. K., Singh, T., Kayshap, P., & Srivastava, A. K. 2018b, in IAU Symp. 340, Long-term Datasets for the Understanding of Solar and Stellar Magnetic Cycles (Cambridge: Cambridge Univ. Press), 237
Morgan, H., & Druckmüller, M. 2014, SoPh, 289, 2945
Ofman, L., & Thompson, B. J. 2011, ApJL, 734, L11
Okamoto, T. J., Tsuneta, S., Berger, T. E., et al. 2007, Sci, 318, 1577
Olson, B. J., Larsson, J., Lele, S. K., & Cook, A. W. 2011, PhFl, 23, 114107
Pant, V., Datta, A., & Banerjee, D. 2015, ApJL, 801, L2
Parenti, S. 2014, LRSP, 11, 1
Priest, E. 2014, Magnetohydrodynamics of the Sun (Cambridge: Cambridge Univ. Press)
Priest, E. R. 1989, Dynamics and Structure of Quiescent Solar Prominences, Astrophysics and Space Science Library, Vol. 150 (Dordrecht: Kluwer Academic), 150
Rayleigh, Baron (John William Strutt) 1899, Scientific Papers (Cambridge: Cambridge Univ. Press)
Ruderman, M. S., Terradas, J., & Ballester, J. L. 2014, ApJ, 785, 110
Ryutova, M., Berger, T., Frank, Z., Tarbell, T., & Title, A. 2010, SoPh, 267, 75
Schmieder, B., Chandra, R., Berlicki, A., & Mein, P. 2010, A&A, 514, A68
Stellmacher, G., & Wiehr, E. 1973, A&A, 24, 321
Stone, J. M., & Gardiner, T. 2007, ApJ, 671, 1726
Su, Y., Veronig, A. M., Hannah, I. G., et al. 2018, ApJL, 856, L17
Tandberg-Hanssen, E. 1998, in IAU Coll. 167, New Perspectives on Solar Prominences, ed. D. F. Webb, B. Schmieder, & D. M. Rust (San Francisco, CA: ASP), 11
Taylor, G. 1950, RSPSA, 201, 192
van Ballegooijen, A. A., & Cranmer, S. R. 2010, ApJ, 711, 164
Yardley, S. L., Green, L. M., Williams, D. R., et al. 2016, ApJ, 827, 151
Ye, W. H., Wang, L. F., Xue, C., Fan, Z. F., & He, X. T. 2011, PhPl, 18, 022704
Zhang, W., Wu, Z., & Li, D. 2005, PhPl, 12, 042106
Zhou, Y. 2017a, PhR, 720, 1
Zhou, Y. 2017b, PhR, 723, 1